Iraqi Journal of Physics, 2026 **Vol.24, No.2, PP.21-31**
https://doi.org/10.30723/ijp.v24i2.1533 **P-ISSN: 2070-4003**
E-ISSN: 2664-5548

Tailoring AgO-Doped CdS Nanostructures on Porous Silicon via PLD for High-Performance H_2S and NO_2 Gas Sensors

Mays K. Awais[1], Haitham T. Hussein[1*], and Adi M. Abdul Hussien[1]
[1]*Department of Physics, College of Applied Science, University of Technology, Baghdad, Iraq*
[*]**Corresponding author:** haitham.T.hussein@uotechnology.edu.iq

Abstract

This work presents the fabrication of highly efficient gas sensors based on silver oxide (AgO)- doped cadmium sulfide (CdS) nanostructures deposited on porous silicon (PS) substrates using pulsed laser deposition (PLD). Three doping concentrations of AgO (5, 10, and 15%) were investigated to evaluate their influence on the structural, optical, and gas sensing properties of CdS. The prepared films were characterized using X-ray diffraction (XRD), field emission scanning electron microscopy (FESEM), atomic force microscopy (AFM), UV–Vis spectroscopy, and Fourier transform infrared spectroscopy (FTIR). The XRD results confirmed enhanced crystallinity with increasing AgO concentrations, while FESEM and AFM analyses revealed a nanostructured surface with increased roughness and active surface area. UV–Vis measurements showed a reduction in the optical band gap upon AgO incorporation, whereas FTIR spectra confirmed the successful formation of AgO:CdS heterostructures. Gas-sensing measurements demonstrated that the CdS with 5% AgO sensor exhibited the highest NO_2 sensing response of 92.8% at an operating temperature of 100°C. The enhanced sensing performance is attributed to the synergistic effect of AgO/CdS heterostructure formation, increased adsorption sites, and improved charge transfer through the PS substrate. The developed AgO:CdS/PS platform offers tunable sensing behavior by controlling dopant concentration and operating temperature, making it a promising candidate for high-performance toxic gas sensing applications.

Article Info.

Keywords:
Gas Sensor, CdS Nanoparticles, AgO Doping, Porous Silicon, Pulse Laser Deposition.

Article history:
Received: Dec. 06, 2025
Revised: Mar. 05, 2026
Accepted: Mar. 15, 2026
Published: Jun. 01, 2026

1. Introduction

Hydrogen sulfide (H_2S) and nitrogen dioxide (NO_2) are the most commonly toxic environmental contaminants released during industrial processes and fossil-fuel combustion [1-3]. Epidemic exposure to toxic gases in air pollution [4, 5] has become a major concern, both environmental and health-wise, in the modern world. These gases, even at very low concentrations, can be harmful to human health and ecological systems, so their early detection is critical for environmental protection and public safety. Semiconductor nanomaterials-based solid-state gas sensors have received wide attention due to their high sensitivity, rapid response, small size, and low cost. Cadmium sulfide (CdS) has a preferable energy band gap and strong surface reactivity; hence, CdS-based nanostructures have been used for gas sensing applications [6, 7]. As a result, silver-based oxides, including silver oxide (AgO), have been fabricated to improve sensing properties via catalytic activity and heterojunction [8]. Porous silicon (PS) substrates, on the other hand, have been found beneficial in enhancing sensor response by increasing surface area and facilitating gas diffusion and charge transport [9-11].

CdS is a II-VI semiconductor and has a direct optical bandgap of about 2.4 eV, making it the best candidate for gas sensing and optoelectronic applications. Nevertheless, the sensing performance of pure CdS is often limited by its low density of surface adsorption sites and poor charge transport, which restricts gas-surface interactions and decreases sensor response [12-14]. To address these limitations, various dopants and secondary phases (metal oxides) have been incorporated into CdS to improve its electronic structure, surface reactivity, and, consequently, catalytic performance. Among these materials, AgO is a p-type semiconductor characterized by its narrow band gap and mixed valence states (Ag^{+}/Ag^{3+}), which are remarkably beneficial to catalytic behavior as well as the charge transfer process [15, 16]. Formation of AgO:CdS heterojunctions can greatly enhance the gas-sensing performance by promoting the separation of electrons and holes, increasing the number density of active adsorption sites, and accelerating surface redox reactions with target gas molecules [17]. Furthermore, PS is used as a substrate, which not only increases the effective surface area and adsorption but also enhances electrical conductivity, promoting gas diffusion of gas, and facilitating charge transport in the sensing layer. Although both AgO-based and CdS-based sensors have been extensively investigated, the coupled AgO: CdS heterostructure adapted on PS has been underexplored with respect to tunable gas-sensing performance controlled by dopant concentration and operating temperature [18, 19]. Such systematic research opportunities are distinctly lacking in the recent development of multifunctional gas sensors.

In this work, the deposition, using pulsed laser deposition, of AgO-doped CdS nanostructured films on PS substrates is presented to form a tunable sensing platform for toxic gas detection. The microstructural, optical, and sensing properties were systematically tailored by varying the AgO concentration. As such, the novelty lies in the fact that this study indicates that optimized and selective detection of different gases could be realized using only one AgO:CdS/PS system by tuning material engineering and operating conditions, which is hoped to offer a novel route for designing an energy-performance gas sensor.

2. Experimental

A porous Si layer was attained using an n-type Si wafer with a thickness of 550 µm and an electrical resistivity of 2-10 Ω.cm. A laboratory-made photo-electrochemical etching design was utilized to produce a porous layer, with a gold mesh serving as the cathode and an n-type Si wafer as the anode. The prepared etching solution contained 99.99% pure ethanol with 48% hydrofluoric acid (HF) of 10% concentration in a Teflon electrochemical cell. Herein, a 150-Watt tungsten light was employed throughout the Si etching process. The utilized Si substrates were cut into 2 × 2 cm^2, then placed in an ethanol-based ultrasonic bath for about 30 minutes to remove surface impurities. The etching procedure was performed for 15 minutes at a 10% HF, and a current density of 20 mA/cm^2. The surface tension was mainly reduced by utilizing ethanol during the etching process, thereby achieving uniformity and homogeneity in the porous Si film.

The deposition target was attained using both cadmium sulfide (CdS, 99% purity, supplied by Sigma-Aldrich, USA) and silver oxide (AgO of 98% purity, supplied by Hongwu International Group Ltd, China), with different doping concentrations. The first target was obtained using 3 g of CdS, while the subsequent targets were acquired with AgO doping ratios of 5, 10, and 15%. The targets were obtained under mechanical pressure of 3 tons for 30 minutes. Once accomplished, the target was vertically aligned and positioned 10 cm from the porous Si substrate, in a vacuum chamber for the PLD process. The placed target was then irradiated with a 532 nm picosecond pulsed laser of a frequency of 6 Hz and a pulse duration of 10 ns; the laser energy was fixed at 180 mJ, and 200 pulses. Fig. 1 depicts the deposition setup utilized in this study.

The morphologies of the samples were investigated using Field-Emission Scanning Electron Microscopy (FESEM)(TESCAN- MIRA3, made in the Czech Republic). The crystal structure of materials was determined by X-ray diffraction (XRD, Shimadzu-XRD6000, Japan). The X-ray wavelength was 0.15406 nm, using Cu-Kα source radiation. The optical properties were measured using a UV-Vis spectrophotometer (Cary 100 CONC plus). The Atomic Force Microscope (AFM) topographies were obtained using digital instruments (Workshop TT-20; the FTIR measurements were performed in a spectrum range between (450-4000) cm^{-1} for the prepared sample.

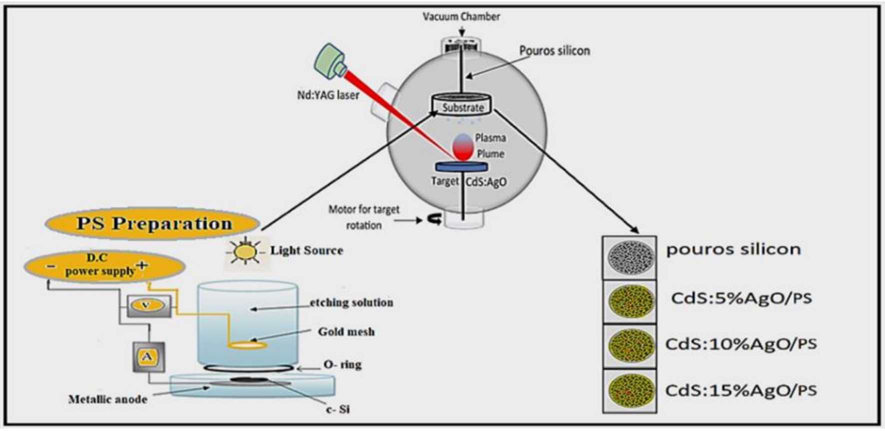

Figure 1: Schematic representation of the electrochemical etching and deposition set-up[20].

To evaluate the sensitivity of the fabricated H_2S and NO_2 gas sensors, particularly the response and recovery times, a gas-sensing setup was employed, as shown in Fig. 2. The system consists of a cylindrical stainless-steel chamber with an effective volume of 6594 cm^3, equipped with a gas inlet and air admittance valves. Electrical connections to the sensor electrodes, heater, and K-type thermocouple were established through a multi-pin feedthrough at the chamber base. The sensor operating temperature was controlled using an internal hot plate, and a thermocouple was used to systematically vary the temperature at (25, 100, 200 and 300 °C). Changes in the sensor current upon exposure to air–NO_2 gas mixtures were recorded using a PC-interfaced digital multimeter (UNI-T UT81B). The test gas was generated by mixing zero air with the target gas, with flow rates regulated by a flow meter and a needle valve; a fixed gas concentration of 30 ppm was introduced directly over the sensor inside the chamber to ensure accurate sensitivity measurement [21, 22]. The gas sensor sensitivity (S) was calculated using Eq. (1):

$$S = \frac{|\mathrm{Igas} - \mathrm{Iair}|}{\mathrm{Iair}} \qquad (1)$$

where I_{air} and I_{gas} represent the sensor current measured in air and upon exposure to the target gas, respectively [23].

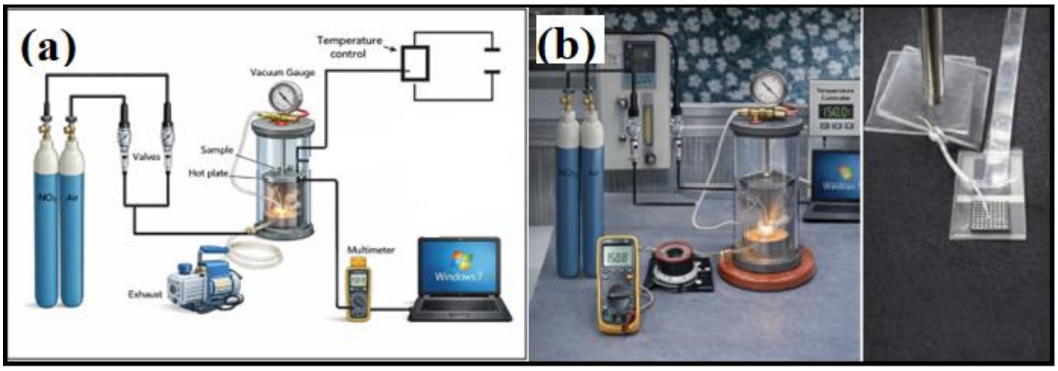

Figure 2: (a) Schematic illustration of the gas sensor testing system, (b) photograph of the fabricated sensor mounted inside the test chamber.

3. Results and Discussion

Fig. 3 displays the XRD patterns of the deposited layers (porous Si, CdS, AgO, and 10% AgO-doped CdS). Fig. 3a shows a sharp diffraction peak at 2θ ≈ 69.12°, corresponding to the 111-crystal plane, indicating the high crystallinity and purity of the prepared porous Si layer. The narrow, high-intensity peak designates the uniformity of the crystal structure. Fig.

3b shows the diffraction peaks of the deposited CdS nanoparticles at 2θ values of 26.52°, 43.91°, 52.14°, and 70.70°, corresponding to the 111, 020, 022, and 311 crystal planes, respectively. These peaks are in good agreement with the standard values for face-centered cubic CdS nanoparticles phase (JCPDS No. 10-0454). The presence of these sharp peaks specifies that the deposited film has upright crystallinity. Fig. 3c shows the XRD patterns of AgO peaks attained at 2θ angles of 21.74, 32.84°, 35.64, 38.34°, 44.39°, 64.47°, and 77.74 corresponding to the planes 210, 122, 111, 111, 200, 220, and 311, respectively, indicating the monoclinic AgO crystal phase according to JCPDS No. 41-1104. The height of the peak at 2θ ≈ 35.64° for the 111-crystal plane specifies that crystal growth is preferred in this direction, reflecting the high crystal consistency as well as distinct orientation of the crystal for the deposited nano-scaled film. The outcomes of the 10% AgO doped CdS layer are demonstrated in Fig. 3(d), distinct peaks corresponding to the CdS crystalline planes, along with additional peaks attributed to the AgO nanoparticles phase. A shift in the CdS peaks was observed in the XRD patterns. This performance could be explained by the lattice strain in the CdS crystal lattice, while a reduction in the AgO peaks intensity could be attributed to the slight dissimilarities in oxidation ratios, the formation of mixed AgO nanoparticles, or background noise that obscures their visibility [24].

The PS layer analysis using AFM (Fig. 4a) demonstrates surface inhomogeneity with well-defined peaks, whose height N varies to about 23.13 nm on average, as shown in Table 1. The plastic characteristics, when mapped, show moderate surface roughness attributed to non-homogeneous molecule accumulation and asymmetric growth features of the coating deposits. The related roughness parameters were: mean roughness, Sa = 2.60 nm; RMS roughness, Sq = 3.69 nm, which reflect a consistent surface spatial frequency; however, they confirm the irregular nature of the PS layer more clearly than any other single property.

In comparison, the surface morphology of the AgO thin film, shown in Fig. 4b, is more homogeneous and compact than that formed with Ag plating alone, even though it has a larger maximum peak height of Sp ≈ 25.93 nm. Lower Sa values of 1.95nm and Sq of 2.68nm (Table 1) indicate that the surface became more uniform, with less scattering, and that a higher packing density of nanoparticles occurred, indicating the formation of a stable, ordered nanostructured layer. These results indicate an ideal surface with a highly crystalline structure and reduced surface defects, representing the most stable form.

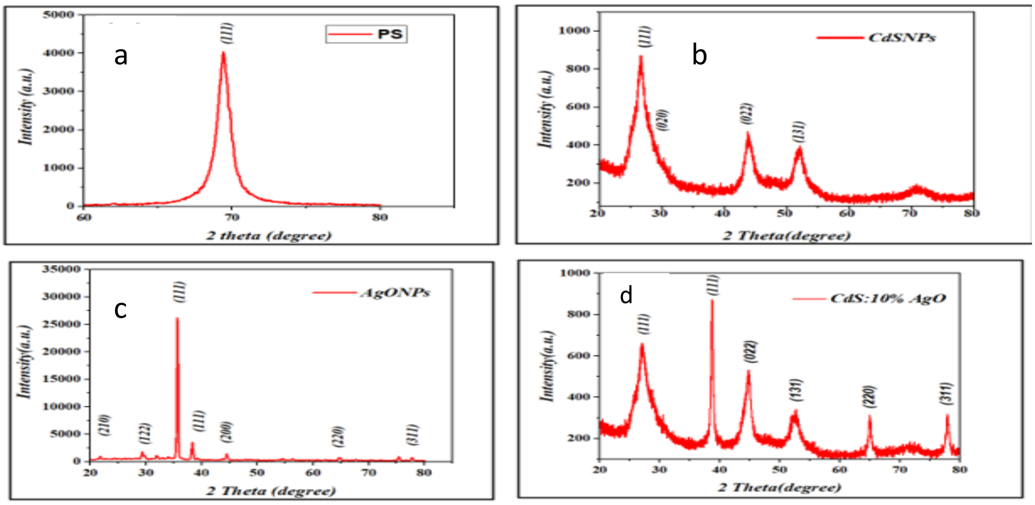

Figure 3: XRD patterns of (a) PS, (b) CdS, (c) AgO, and (d) CdS:10%AgO.

Table 1: the AFM-derived surface roughness parameters, including (Sa, Sq, and Sp) of PS, AgO, and CdS layers.

Samples	Mean Sa (nm)	RMS (Sq) (nm)	Maximum Sp (nm)
PS	2.60469	3.69058	23.1271
AgO	1.94726	2.67560	25.9326
CdS	3.36475	4.85714	31.6170

In addition, the CdS layer (Fig. 4c) shows a significantly rougher surface with prominent height deviations of about 31.62 nm at peak height (Table 1). The increased roughness (Sa = 3.36 nm and Sq = 4.86 nm) is explained by grain growth and partial agglomeration of nanoparticles during deposition. The dual zigzag surface topology increases the effective surface area, thereby promoting enhanced gas adsorption via increased interactions and scattering of gas molecules on the roughened scraggy landscape, corroborating with earlier reports [25].

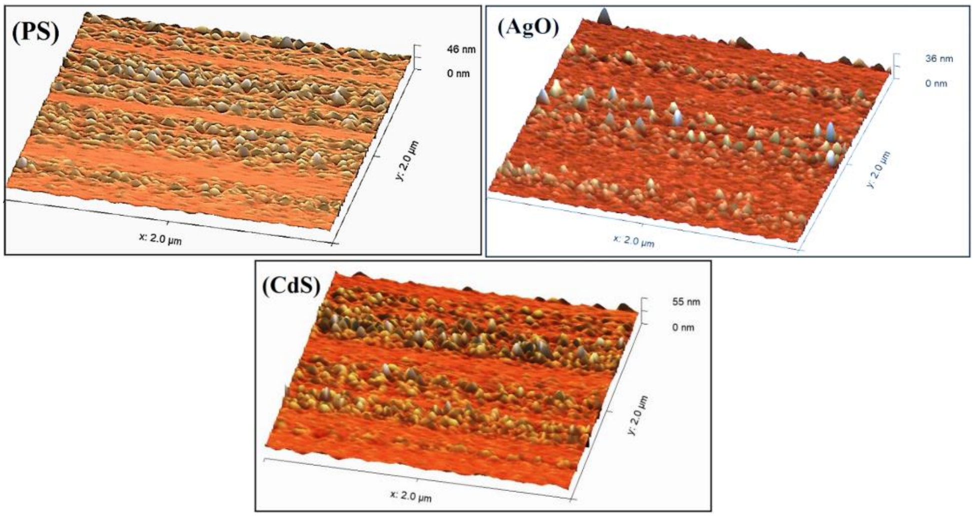

Figure 4: AFM topographies of (a) porous Si, (b) AgO, and (c) CdS nanostructured layers.

The Field emission scanning electron microscopy (FESEM) images in Fig. 5 show the surface structure of the samples deposited on a PS substrate. The image of the PS surface shows a three-dimensional porous network with large pores, allowing rapid diffusion of gas molecules and facilitating efficient concentration, thereby enhancing the performance of the gas layers.
In the case of the CdS/AgO composite, the FE-SEM images reveal a homogeneous distribution of nanoscale structures over the PS framework. At a low 5% AgO doping concentration, AgO nanoparticles are uniformly decorated on the CdS grains, leading to an increased surface roughness and a higher surface-to-volume ratio, which enhances the density of active adsorption sites and facilitates efficient charge transfer across the CdS/AgO heterointerfaces. At an intermediate AgO concentration (10% AgO), a more continuous and well-interconnected nanostructured network is formed, providing an optimal balance between heterojunction density and pore accessibility, which is beneficial for charge transport and gas diffusion. With further increasing of AgO content to 15%, partial agglomeration of AgO nanoparticles is observed, resulting in a relatively denser surface morphology and partial coverage of the PS pores, which may limit gas diffusion pathways despite the increased number of heterointerfaces. Nevertheless, the PS substrate maintains a crucial role by providing a high density of interconnected nanochannels and a large internal surface area, thereby promoting charge transport, suppressing carrier recombination, and contributing significantly to the overall performance and stability of the CdS/AgO nanostructured layers.

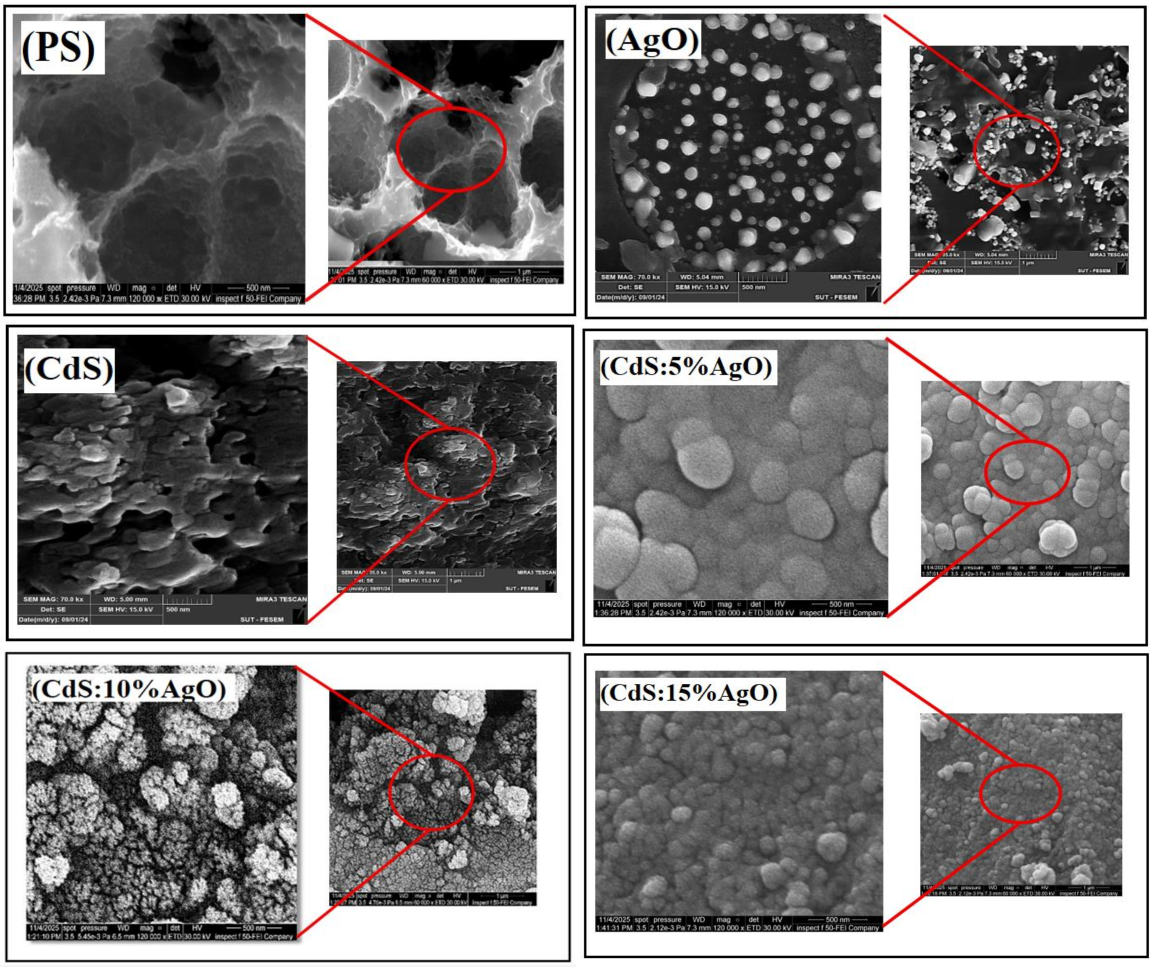

Figure 5: FESEM images of PS, AgO, CdS, and AgO-doped CdS nanostructures.

Fig. 6 reveals the absorption spectra of both CdS and AgO nanostructured layers, showing strong absorption peaks in the UV region at wavelengths around 200-300 nm, associated with band-to-band electronic transitions. A decrease in absorption intensity toward longer wavelengths is observed, which has been correlated in the literature with a reduced density of surface defects and improved crystallinity, as fewer defect states contribute to sub-bandgap absorption [26]. Based on the Tauc plot analysis attached to the figures, the optical gap (E_g) was determined for each material to be approximately 2.27 eV for CdS and 2.81 eV for AgO, consistent with standard values for nanomaterials. The slight shift in the absorption edge is attributed to the quantum confinement effect arising from the small size of the nanoparticles, which leads to an increase in the optical gap energy. These results indicate that the prepared materials possess enhanced nano-optical properties, making them suitable for gas and light-sensing applications due to their high spectral response and efficient charge separation.

The FTIR spectra in Fig. 7 show the vibrational extensions of the active aggregates on the surfaces of the samples prepared from AgONPs and CdSNPs in the range (4000–500 cm^{-1}). An absorption band is observed at approximately 3400 cm^{-1}, attributed to O-H group vibrations resulting from moisture absorption or the presence of water molecules on the surface. A band also appears at 1630-1650 cm^{-1}, indicating N-H or C=O vibrations of organic compounds remaining from the preparation agents.

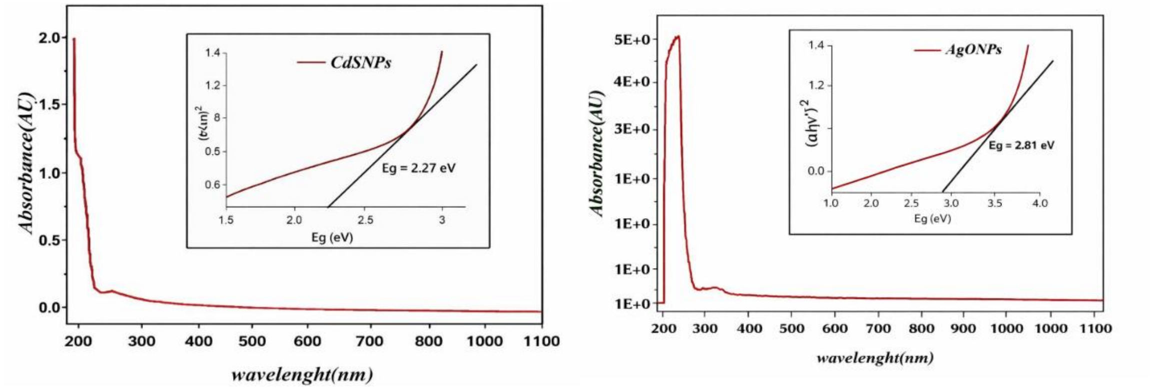

Figure 6: Optical analysis of the deposited CdS and AgO nanostructured layers.

The peaks at 2850-2920 cm^{-1} are due to C-H vibrations, while for CdS, a band is observed at 1040–1100 cm^{-1}, attributed to C-O or SO vibrations, indicating surface sulfur-oxygen bonds. In AgO, a distinct peak appears at ~470 cm^{-1}, due to Ag-O bond vibrations, confirming the formation of the AgO phase. These results indicate that the prepared materials contain multiple active groups, which improve surface interaction when used as gas sensors. O-H, C-O, and M-O bonds (M = Cd, Ag) act as active centers for gas adsorption and enhanced sensory response.

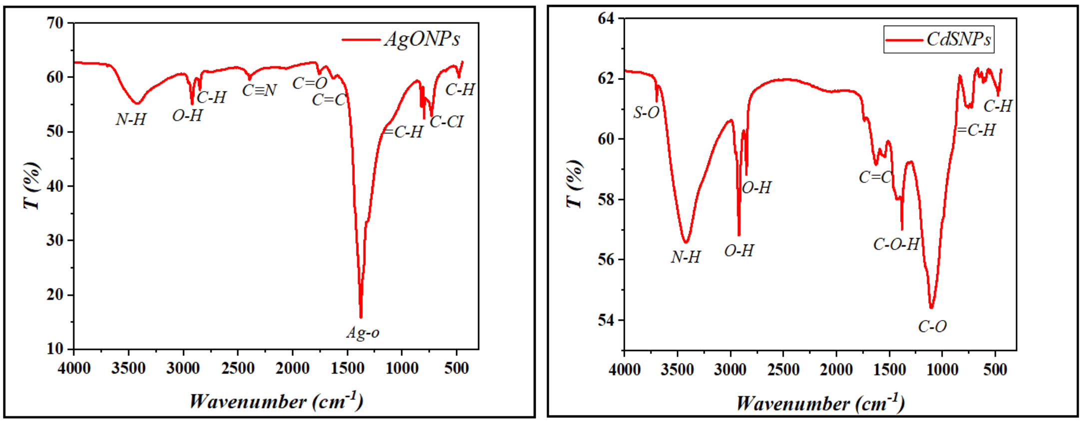

Figure 7: FTIR spectra of the deposited AgO and CdS nano-scale layers.

The curves in Fig. 8 show the relationship between operating temperature and the sensitivity of gas sensors prepared from AgO-doped CdS at different doping concentrations (5, 10, and 15%), compared to the undoped sample and the sample deposited on PS. Fig. 8a shows that the sensitivity of the AgO-doped CdS sensor to NO_2 gas is highly dependent on the doping concentration and temperature. The sample doped with 5% AgO exhibited the highest gas response, reaching its maximum sensitivity at an operating temperature of approximately 100°C, then gradually decreasing with increasing temperature. This behavior is attributed to the increased number of active sites on the surface of the sample for the adsorption of NO_2 molecules, which leads to increased electron accumulation in the conduction band as a result of the NO_2 gas-electron acceptor interaction. As the temperature increases, the adsorbed molecules begin to desorb from the surface, reducing the number of transferred charges and thus decreasing sensitivity. This performance also indicates that the 5% doping provides an ideal balance between enhanced surface adsorption and charge transfer at low temperatures. Fig. 8b shows the response to H_2S gas; the results show the highest sensitivity for the sample doped with 5% AgO at an operating temperature of approximately 25 °C. This can be explained by the fact that H_2S gas is a reducing gas, which reacts with the oxygen adsorbed on the sample surface, releasing additional electrons into the conduction band and increasing electrical conductivity. As the temperature increases, molecular mobility and the speed of surface reactions increase, enhancing the sensor response until the optimum temperature is reached, after which sensitivity begins to decline due to reduced stable adsorption of the gas to the surface. The doping ratio plays a pivotal role in determining sensor performance. Moderately high AgO content (5-15%) leads to the formation of CdS/AgO heterojunctions, which contribute to enhanced electron and hole separation and reduced recombination, thus enhancing gas response efficiency. Conversely, low or excessive doping may result in decreased sensitivity due to fewer active sites or increased electron scattering [27].

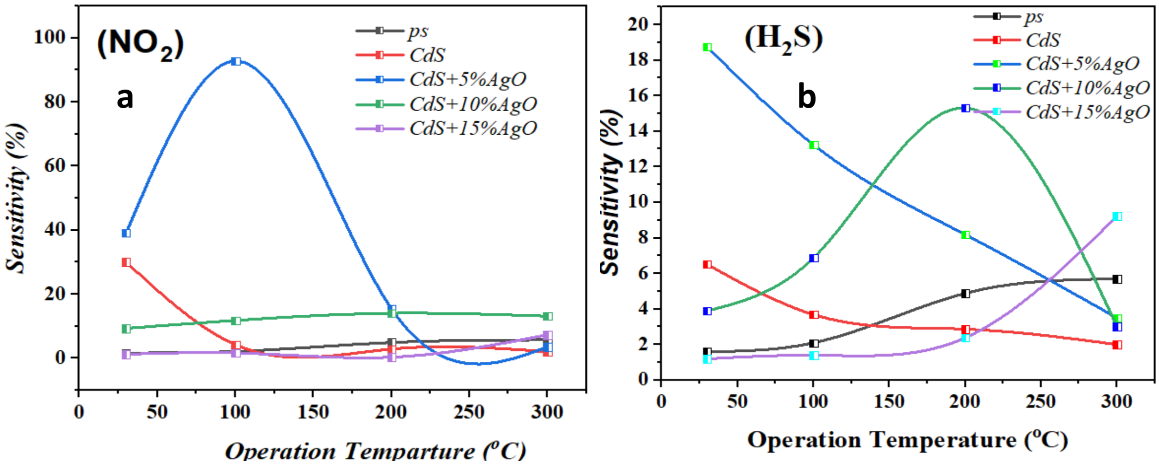

Figure 8: Sensor sensitivity toward (a) NO_2 and (b) H_2S at different operating temperatures.

Fig. 9 shows the variation of response and recovery times of pure CdS and AgO-doped CdS sensors (5, 10, and 15%) toward H_2S and NO_2 gases as a function of operating temperature. It is evident that both the operating temperature and the dopant concentration significantly influence the sensing kinetics. For both gases, the 5% AgO-doped CdS sensor exhibits a balanced behavior, showing relatively short response and recovery times over a wide temperature range, while maintaining high sensitivity. This can be attributed to the optimal dispersion of AgO nanoparticles on the CdS surface, which increases the density of active adsorption sites and oxygen vacancies, thus enhancing gas–surface interaction and charge transfer. In contrast, the 10% AgO-doped sample shows the fastest response and recovery times, particularly at moderate operating temperatures. This behavior is related to the increased charge carrier concentration and improved electrical conductivity induced by higher AgO content, which accelerates electron transport during gas adsorption and desorption. However, excessive doping partially blocks active sites and reduces the effective surface area, resulting in a lower gas response than in the 5%-doped sample. For the 15% AgO-doped sample, the response and recovery times become slower, which can be attributed to dopant agglomeration and the formation of insulating regions that hinder gas diffusion and charge transport. Therefore, although the 10%-doped sensor exhibits faster dynamics, the 5% AgO-doped CdS sample offers the best compromise between surface reactivity and charge transport, making it the optimal composition for gas-sensing applications.

The gas-sensing performance of the CdS/AgO-based sensors reported in this work was compared with that of previously reported CdS-based gas sensors in the literature. The proposed sensors exhibit comparable or improved sensitivity at lower operating temperatures. In particular, the CdS:5% AgO sensor demonstrates enhanced sensing performance at moderate temperatures, whereas many reported CdS-based sensors require higher operating temperatures to achieve similar responses. This improvement can be attributed to the effective role of AgO in increasing the number of active adsorption sites and facilitating charge transfer at the gas–sensor interface.

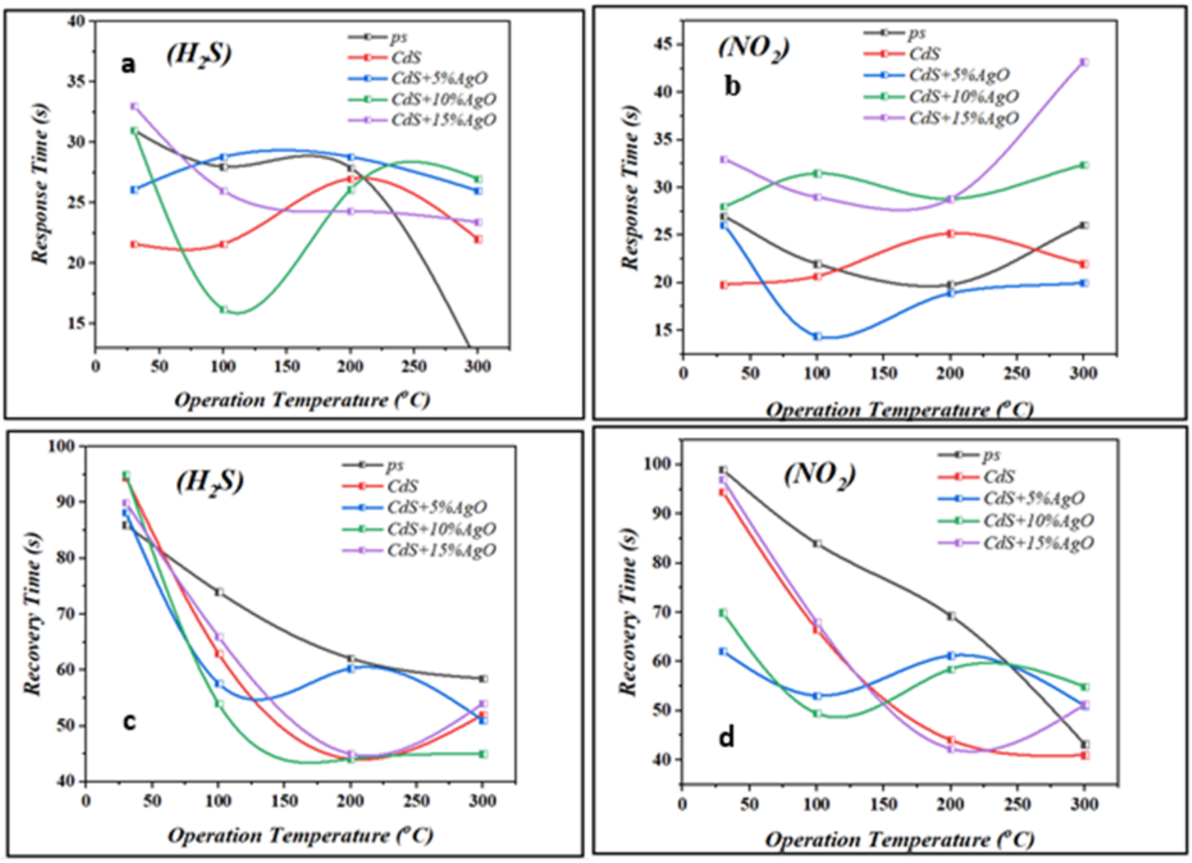

***Figure 9:** Response and recovery times of CdS/AgO gas sensors toward H_2S and NO_2 at different operating temperatures.*

Therefore, the present results indicate that the developed CdS/AgO sensors offer a competitive advantage in terms of sensitivity and operating temperature compared with other reported gas sensing materials. Compared with similar reported geometries, the proposed system exhibited outcomes comparable to those of other structures (Table 2).

Table 2: Comparison of the fabricated gas sensor to other reported similar geometries.

Samples	Temperature (°C)	Gas Concentration (ppm)	T_{rise} / T_{fall} (sec.)	Sensitivity (%)	Ref.
SnO_2/CdS	200	5000	40/110	44	[24]
CdS/RGO	-	1000	10/22	2.23	[25]
CdS/TiO_2	RT	100	68/74	69.16	[26]
NiO/CdS-CdO	>200	100	47/66	21.5	[27]
AgO/CdS	100	30	57/51	85.33	This work

4. Conclusions

In this work, gas sensors were developed by depositing CdS, AgO, and their composites on a PS substrate to enhance adsorption and charge-transfer properties for sensing NO_2 and H_2S gases. SEM results revealed a regeneratively sensitive nanostructure in the CdS:5%AgO/PS sample, characterized by an increased effective surface area for gas diffusion within the PS's permeate channels. This was reflected in the improved sensor performance, with the CdS:5%AgO/PS sample achieving the highest speed, signal recovery, and signal strength compared to other samples. This indicates the effectiveness of the synergistic mechanism between CdS and AgO in reducing electron recombination and electron transfer across hybrid junctions. Completely, CdS:5%AgO/PS can be classified as the ideal candidate for a gas sensor for both oxidizing and reducing gases. This study also outlines future work to improve selectivity, reduce operating temperature, and investigate its long-term performance, making this system a valuable and effective alternative in the field of advanced sensors.

Conflict of Interest

The authors declare that they have no conflict of interest.

References

1. B. Zong, S. Wu, Y. Yang, Q. Li, T. Tao and S. Mao, Smart gas sensors: recent developments and future perspectives, *Nano-Micro Lett*. **17**(1), 54 (2025). https://doi.org/10.1007/s40820-024-01543-w.
2. H. Zhang, D. Zhang, Y. Yang, L. Zhou, Y. Liu, W. Liu, Y. Sun, Y. Guo and Y. Ji, Eco-friendly triboelectric nanogenerator for self-powering stacked In_2O_3 nanosheets/PPy nanoparticles-based NO_2 gas sensor, *Nano Energy*. **128**(B), 109978 (2024). https://doi.org/10.1016/j.nanoen.2024.109978.
3. M.H. Kareem, H.T. Hussein, and A.M. Abdul Hussein, Study of the effect of CNTs, and (CNTs-ZnO) on the porous silicon as sensor for acetone gas detection, *Optik*. **259**, 168825 (2022). https://doi.org/10.1016/j.ijleo.2022.168825.
4. A. Vaidyanathan, B. Mondal, C.S. Rout and B. Chakraborty, Plasmonic gas sensors based on nanomaterials: mechanisms and recent developments, *J. Phys. D: Appl. Phys.*, **57**(26), 263002 (2024). https://doi.org/10.1088/1361-6463/ad32a7.
5. Y. Yin, Y. Liu, Y. Wang, Y. Cheng, Y. Li, G. Cao, H. Zong, M. Li, L. Yan and B. Zhang, SnO_2/carbon dots nanocomposite synthesized by one-pot solvothermal technique for high-sensitivity triethylamine gas sensors, *Solid State Ion*. **407**, 116498 (2024). https://doi.org/10.1016/j.ssi.2024.116498.
6. S. Wakita, Y. Masuda, P.G. Choi, T. Matsuoka, Y. Harada and S. Takami, Semiconductor-Type Gas Sensors Based on Surface-Modified Iron Oxide Nanoparticles for ppb-Level Detection of Acetone, *ACS Appl. Electron. Mater.* **7**(18), 8550 (2025). https://doi.org/10.1021/acsaelm.5c01355.
7. M.H. Kareem, A.M. Abdul Hussein and H.T. Hussein, Preparation high quality ethanol gas sensor by modifying porous silicon (PS) surface with carbon nanotube (CNTs), *Optik*, **259**, 168826 (2022). https://doi.org/10.1016/j.ijleo.2022.168826.
8. S.M. Kheder, H.T. Hussein and H.M. Alattar, Novel CdS/MWCNTs/CuO nanocomposite with high photocatalytic and antimicrobial activity, *Indian J. Phys.*, **99**, 3805 (2025). https://doi.org/10.1007/s12648-025-03581-5
9. H. Ullah, R. Ahmad, A.A. Khan, N. Khaliq, M. Khan, G. Ali, S. Karim, X. Yi and S.O. Cho, A sensitive non-enzymatic glucose sensor based on MgO entangled nanosheets decorated with CdS nanoparticles: Experimental and DFT study, *J. Mol. Liq.* **360**, 119366 (2022). https://doi.org/10.1016/j.molliq.2022.119366.
10. H. Nazemi, A. Joseph, J. Park and A. Emadi, Advanced micro-and nano-gas sensor technology: A review, *Sens.* **19**(6), 1285 (2019). https://doi.org/10.3390/s19061285.
11. A. Sukee, A.A. Alharbi, A. Staerz, A. Wisitsoraat, C. Liewhiran, U. Weimar and N. Barsan, Effect of AgO loading on flame-made $LaFeO_3$ p-type semiconductor nanoparticles to acetylene sensing, *Sens. Actuators B: Chem.* **312**, 127990 (2020). https://doi.org/10.1016/j.snb.2020.127990.
12. E.T. Salim, M.H. Amin, Z.T. Salim, J.A. Saimon, E.Y. Salih, A.A. Al-Amiery and S.C.B. Gopinath, Enhanced gas sensing properties using Ag@WO_3 core–shell nanoparticle prepared using liquid phase laser ablation, *J. Mater. Sci: Mater. Electron.* **36**(26), 1695 (2025). https://doi.org/10.1007/s10854-025-15763-2.
13. S.S. Mughal and S.M. Hassan, Comparative study of AgO nanoparticles synthesize via biological, chemical and physical methods: A review, *Am. J. Mater. Synth. Process.* **7**(2), 15 (2022). https://doi.org/10.11648/j.ajmsp.20220702.11.
14. A. Rita, A. Sivakumar, S.S.J. Dhas and S.A.M.B. Dhas, Structural, optical and magnetic properties of silver oxide (AgO) nanoparticles at shocked conditions, *J. Nanostruct. Chem.* **10**(4), 309 (2020). https://doi.org/10.1007/s40097-020-00351-z.
15. N.K. Abdalameer, K.A. Khalaph and E.M. Ali, Ag/AgO nanoparticles: Green synthesis and investigation of their bacterial inhibition effects, *Mater. Today: Proc.* **45**(6), 5788 (2021). https://doi.org/10.1016/j.matpr.2021.03.166.
16. M.S. Majeed, S.M.M. Mahmoud, R.M. Rasheed and A.A. Rashad, Synthesis AgO Nanoparticles by Nd:Yag Laser with Different Pulse Energies, *Baghdad Sci. J.* **21**(1), 0217 (2024). https://doi.org/10.21123/bsj.2023.7539.
17. A. B. de Paiva, L. M. B. Vargas, M. J. da Silva, A. D. G. Rodrigues, D. A. W. Soares, M. L. Peres, and M. P. F. de Godoy, The negative photoconductivity of Ag/AgO grown by spray-pyrolysis, *Surf.* **5**(1), 209 (2022). https://doi.org/10.3390/surfaces5010014.

18. A. Sobhani-Nasab and M. Behpour, Synthesis and characterization of AgO nanostructures by precipitation method and its photocatalyst application, *J. Mater. Sci: Mater. Electron.* **27**(2), 1191 (2016). https://doi.org/10.1007/s10854-015-3873-7.
19. G. Korotcenkov, Metal oxides for solid-state gas sensors: What determines our choice? *Mater. Sci. Eng. B*, **139**(1), 1 (2007). https://doi.org/10.1016/j.mseb.2007.01.044.
20. N. Zhang, X. Ma, S. Ruan, Y. Yin, C. Li, H. Zhang, and Y. Chen, Excellent gas sensing of CdS nanowires decorated with Ag nanoparticles, *J. Nanosci. Nanotechnol.* **19**(11),7083 (2019). https://doi.org/10.1166/jnn.2019.16720.
21. S. Deb, R. Kumar, A. Singh, and P. Sharma, Review on development of metal-oxide and 2D material-based gas sensors, *Curr. Opin. Solid State Mater. Sci.* **30**, 101160 (2024). https://doi.org/10.1016/j.cossms.2024.101160.
22. S.F.Pichorim, N.J.Gomes, J.C.Batchelor. Two Solutions of Soil Moisture Sensing with RFID for Landslide Monitoring. *Sens.* **18**(2), 452 (2018). https://doi.org/10.3390/s18020452.
23. S. Kumar, A. U. Rao, A. K. Chawla, and S. Awasthi, Exploring the role of metal oxide heterostructures for next-generation gas sensors: A focus on NH_3, H_2S and NO_2 gases, *Chem. Phys. Impact.* **100986**,100986 (2026). https://doi.org/10.1016/j.chphi.2025.100986.
24. L. Yadava, R. Verma, and R. Dwivedi, Sensing properties of CdS-doped tin oxide thick film gas sensor, *Sens. Actuators B: Chem.* **144**(1), 37 (2010). https://doi.org/10.1016/j.snb.2009.10.013.
25. A. Hasani, H. Sharifi Dehsari, A. Amiri Zarandi, A. Salehi, F. Afshar Taromi, and H. Kazeroni, Visible light-assisted photoreduction of graphene oxide using CdS nanoparticles and gas sensing properties, *J. Nanomater.*, **2015**(1), 930306 (2015). https://doi.org/10.1155/2015/930306.
26. V. N. Rao, K. S. Pasupuleti, M.-D. Kim, M. Rezakazemi, T. M. Aminabhavi, C. W. Ahn, and J.-M. Yang, CdS/TiO_2 nano hybrid heterostructured materials for superior hydrogen production and gas sensor applications, *J. Environ. Manage.* **340**, 117895 (2023). https://doi.org/10.1016/j.jenvman.2023.117895.
27. M. Hassan, Z. Liang, S. Liu, S. Hussain, G. Qiao, and G. Liu, Temperature-driven n-to p-type transition of a chemiresistive NiO/CdS-CdO NO2 gas sensor, *Sens. Actuators B: Chem.* **398**, 134755 (2024). https://doi.org/10.1016/j.snb.2023.134755.

تحسين البنى النانوية لكبريتيد الكادميوم المطعم بأكسيد الفضة على السيليكون المسامي باستخدام تقنية الترسيب بالليزر النبضي لتصنيع مجسات غازي كبريتيد الهيدروجين و ثنائي اوكسيد النتروجين عالية الأداء

ميس كريم عويز[1] و هيثم طالب حسين[1] وعدي محمود عبد الحسين[1]
[1]قسم الفيزياء، كلية العلوم التطبيقية، الجامعة التكنولوجية، بغداد، العراق

الخلاصة

يتناول هذا العمل تصنيع مستشعرات غاز عالية الكفاءة تعتمد على هياكل نانوية من كبريتيد الكادميوم (CdS) المُطعّم بأكسيد الفضة (AgO)، والمُرسبة على ركائز من السيليكون المسامي باستخدام تقنية الترسيب بالليزر النبضي (PLD). دُرست ثلاثة تراكيز تطعيم لأكسيد الفضة (5%، 10%، و15%) لتقييم تأثيرها على الخصائص البنيوية والبصرية وخصائص استشعار الغاز لكبريتيد الكادميوم. تم توصيف الأغشية المُحضّرة باستخدام حيود الأشعة السينية (XRD)، والمجهر الإلكتروني الماسح ذي الانبعاث الميداني (FESEM)، ومجهر القوة الذرية (AFM)، ومطيافية الأشعة فوق البنفسجية والمرئية، ومطيافية الأشعة تحت الحمراء بتحويل فورييه (FTIR). أكدت نتائج حيود الأشعة السينية زيادة التبلور مع زيادة تركيز أكسيد الفضة، بينما كشفت تحليلات المجهر الإلكتروني الماسح ذي الانبعاث الميداني ومجهر القوة الذرية عن سطح ذي بنية نانوية مع زيادة في الخشونة ومساحة السطح النشطة. أظهرت قياسات الأشعة فوق البنفسجية والمرئية انخفاضًا في فجوة النطاق البصري عند دمج أكسيد الفضة (AgO)، بينما أكدت أطياف الأشعة تحت الحمراء بتحويل فورييه (FTIR) نجاح تكوين البنى غير المتجانسة AgO:CdS. وأظهرت قياسات استشعار الغاز أن مستشعر CdS المحتوي على 5% من AgO حقق أعلى استجابة لاستشعار غاز NO_2 بنسبة 92.8% عند درجة حرارة تشغيل 100 درجة مئوية. يُعزى تحسن أداء الاستشعار إلى التأثير التآزري لتكوين البنية غير المتجانسة AgO:CdS، وزيادة مواقع الامتزاز، وتحسين نقل الشحنات عبر ركيزة السيليكون المسامية. توفر منصة السيليكون المسامية AgO:CdS المطورة سلوك استشعار قابلًا للتعديل من خلال التحكم في تركيز المادة المضافة ودرجة حرارة التشغيل، مما يجعلها مرشحًا واعدًا لتطبيقات استشعار الغازات السامة عالية الأداء.

الكلمات المفتاحية: مستشعر غاز، جسيمات نانوية من كبريتيد الكادميوم، تطعيم أكسيد الفضة، سيليكون مسامي، ترسيب ليزري نبضي.